Acta Mechanica 92, 9–27 (1992)

ACTA MECHANICA

Steady state penetration of elastic perfectly plastic targets

R. Jayachandran and **R. C. Batra**, Rolla, Missouri

(Received March 5, 1991; revised May 7, 1991)

Summary. Steady state axisymmetric deformations of an elastic perfectly plastic target being penetrated by a fast moving rigid cylindrical rod have been analyzed by the finite element method. The target is assumed to obey the von Mises yield criterion and the associated flow rule. Contact between target and penetrator has been assumed to be smooth. A mixed formulation, in which two components of the velocity and four components of the deviatoric stress tensor at each node point, and the hydrostatic pressure at the centroid of an element are taken as unknowns, is employed. This should give a better estimate of tractions acting on the penetrator nose, and hence of the axial resisting force experienced by the penetrator. The effect of the penetrator speed, its nose shape and the elasticity of the target material on the target deformations, and the axial force experienced by the penetrator has been studied. The consideration of elastic effects helps delineate the elastic-plastic boundary in the target.

1 Introduction

An outstanding problem in penetration mechanics is to find, within reasonable resources, whether or not for the given penetrator and target geometries, materials, target support conditions, penetrator speed, and the angle of attack, the target will be perforated or not. If the target is perforated, the speed of the penetrator when it ejects out of the target is of interest. And if the target is not perforated, one will like to know the shape and size of the hole made in the target. This problem has defied a complete solution for many years. We refer the reader to review articles by Backman and Goldsmith [1], Wright and Frank [2], Anderson and Bodner [3], and the books by Zukas et al. [4], Blazynski [5], and MaCauley [6] for a summary of the available literature on ballistic penetration. Awerbuch [7], Awerbuch and Bodner [8], Ravid and Bodner [9], Ravid et al. [10], Forrestal et al. [11], and Batra and Chen [12] have proposed engineering models of different complexity.

In recent years, emphasis has been placed on kinetic energy penetrators, which for terminal ballistic purposes may be regarded as long metal rods travelling at high speeds. For impact velocities in the range of 2 – 10 km/s, incompressible hydrodynamic flow equations can be used to describe adequately the impact and penetration phenomena, because large stresses occurring in hypervelocity impact permit one to neglect the rigidity and compressibility of the striking bodies. Birkhoff et al. [13] and Pack and Evans [14] have proposed models which require the use of the Bernoulli equation or its modification to describe the hypervelocity impact. At ordnance velocities (0.5 – 2 km/s), the material strength becomes an important parameter. Allen and Rogers [15] represented the material strength as a resistive pressure. Alekseevskii [16] and Tate [17], [18] have considered separate resistive pressures for the penetrator and the target and proposed that these equal some multiple of the uniaxial yield stress of the material. However, the multiplying factor was not specified. Tate [19], [20], Pidsley [21], Batra and Gobinath [22], Gobinath and Batra [23], and Batra and Chen [12] have estimated these multiplying factors. Whereas Tate used a solenoid fluid flow model to simulate the steady state penetration process, other investigations relied on a numerical solution of the problem.

We recall that the one-dimensional penetration theories [15]–[18] ignore the lateral motion, plastic flow and the detailed dynamic effects. In an attempt to understand better these approximations, Batra and Wright [24] studied the problem of a rigid cylindrical rod with a hemispherical nose penetrating into a rigid/perfectly plastic target. The target deformations as seen by an observer moving with the penetrator nose tip, were presumed to be steady. Subsequently, Batra and his co-workers [25]–[30] studied the effect of nose shape, strain hardening, strain-rate hardening and thermal softening characteristics of the target material. Batra and Gobinath [22]–[23] have analyzed the steady state penetration problem in which both the target and the penetrator deform.

When the target material is modeled as rigid/perfectly plastic it is likely that the hydrostatic pressure at target points adjoining the penetrator/target interface is increased because of the rigidity of the surrounding target material. Also, computations of stresses and hence tractions on the target/penetrator interface from the finite element solution in which velocities at nodal points are taken as unknowns is less accurate as compared to the nodal velocities. We alleviate these concerns here by including the effect of material elasticity in the problem formulation, and using a mixed finite element formulation in which both the nodal velocities and nodal stresses are taken as unknowns.

2 Formulation of the problem

We use a cylindrical coordinate system with origin attached to the center of the penetrator nose, moving with it at a uniform speed v_0, and positive z-axis pointing into the target, to describe the deformations of the target. These deformations appear to be steady to an observer situated at the origin of this coordinate system, and are governed by the following equations:

Balance of mass: $$\operatorname{div} \boldsymbol{v} = 0, \tag{1}$$

Balance of linear momentum: $$\operatorname{div} \boldsymbol{\sigma} = \varrho(\boldsymbol{v} \cdot \operatorname{grad})\, \boldsymbol{v}, \tag{2}$$

Constitutive relations: $$\boldsymbol{\sigma} = -p\boldsymbol{1} + \boldsymbol{s}, \tag{3}$$

$$\mathring{\boldsymbol{s}} = 2G(\boldsymbol{D} - \boldsymbol{D}^p), \tag{4}$$

$$\boldsymbol{s} = 2\mu(I)\, \boldsymbol{D}^p, \tag{5}$$

where

$$2\mu = \frac{\sigma_0}{\sqrt{3}\, I}, \qquad 2I^2 = \operatorname{tr}(\boldsymbol{D}^{p2}), \tag{6.1, 2}$$

$$\mathring{\boldsymbol{s}} = (\boldsymbol{v} \cdot \operatorname{grad})\, \boldsymbol{s} + \boldsymbol{s}\boldsymbol{W} - \boldsymbol{W}\boldsymbol{s}, \tag{7}$$

$$2\boldsymbol{D} = \operatorname{grad} \boldsymbol{v} + (\operatorname{grad} \boldsymbol{v})^T, \qquad 2\boldsymbol{W} = \operatorname{grad} \boldsymbol{v} - (\operatorname{grad} \boldsymbol{v})^T. \tag{8}$$

Equations (1) and (2) are written in the Eulerian description of motion. The operators grad and div denote the gradient and divergence operators on fields defined in the present configuration. In Eqs. (1)–(8), $\boldsymbol{v}$ is the velocity of a target particle relative to the penetrator, $\boldsymbol{\sigma}$ the Cauchy stress tensor, s its deviatoric part, p the hydrostatic pressure not determined by the deformation history, and an open circle on s indicates the Jaumann derivative defined by Eq. (7) for the steady stress field. Furthermore, G is the shear modulus, D^p the plastic strain-rate, μ defined by Eq. (6.1) may be interpreted as the shear viscosity of the target material, σ_0 is the yield stress in a quasistatic simple compression test, D the strain-rate tensor and W is the spin tensor. Equation (4) expresses Hooke's law written in the rate form and is based on the tacit assumption that the strain-rate has additive decomposition into elastic and plastic parts. We note that Pidsley [21] used the ordinary time derivative rather than the Jaumann rate in Eq. (4). Equation (5) follows from the assumption that the target material obeys von Mises yield criterion and the associated flow rule. However, in Eqs. (3)–(5) we have assumed that a material particle is undergoing elastic and plastic deformations simultaneously. Substitution from Eqs. (5) and (7) into Eq. (4) gives the following differential equation for s:

$$(\boldsymbol{v}\cdot\text{grad})\,\boldsymbol{s}+\boldsymbol{sW}-\boldsymbol{Ws}+(G/\mu)\,\boldsymbol{s}=2G\boldsymbol{D}. \tag{9}$$

We non-dimensionalize variables as follows:

$$\begin{aligned}&\bar{\boldsymbol{\sigma}}=\boldsymbol{\sigma}/\sigma_0, \quad \bar{\boldsymbol{s}}=\boldsymbol{s}/\sigma_0, \quad \bar{p}=p/\sigma_0, \quad \bar{\boldsymbol{v}}=\boldsymbol{v}/v_0, \quad \bar{r}=r/r_0,\\ &\bar{z}=z/r_0, \quad \bar{r}_n=r_n/r_0, \quad \bar{I}=I\,\frac{r_0}{v_0},\end{aligned} \tag{10}$$

where the superimposed bar indicates the non-dimensional variable, the pair (r, z) the cylindrical coordinates of a point, v_0 the uniform penetrator speed, r_0 the radius of the cylindrical part of the penetrator, and $2r_0$ and $2r_n$ equal the length of the principal axes of the ellipsoidal nose in the r and z directions, respectively. Equations (1), (2), and (9), when written in terms of non-dimensional variables become

$$\text{div}\,\boldsymbol{v}=0, \tag{11}$$

$$-\text{grad}\,p+\text{div}\,\boldsymbol{s}=\alpha(\boldsymbol{v}\cdot\text{grad})\,\boldsymbol{v}, \tag{12}$$

$$\boldsymbol{s}+\beta\gamma\big((\boldsymbol{v}\cdot\text{grad})\,\boldsymbol{s}+\boldsymbol{sW}-\boldsymbol{Ws}\big)=\beta\boldsymbol{D}, \tag{13}$$

where

$$\alpha=\frac{\varrho v_0{}^2}{\sigma_0}, \quad \gamma=\frac{\sigma_0}{G}, \quad \text{and} \quad \beta=\frac{1}{2\sqrt{3}\,I} \tag{14}$$

are non-dimensional numbers, and we have dropped the superimposed bars. Henceforth, we will use only non-dimensional variables. Note that α and γ are constants for the given problem, but β varies from point to point in the deforming region. The value of α signifies the importance of inertia forces relative to the flow stress of the material, and that of γ gives the effect of material elasticity. For most metals γ is of the order of 10^{-3}. For a rigid perfectly plastic material γ equals zero. The value of the Weissenberg number $(\beta\gamma)$ varies from 10^{-3} to 10^4 in the deforming region.

We assume that the target/penetrator interface is smooth, and impose on it the following boundary conditions:

$$\boldsymbol{t}\cdot(\boldsymbol{\sigma n})=0, \tag{15}$$

$$\boldsymbol{v}\cdot\boldsymbol{n}=0. \tag{16}$$

Here $\boldsymbol{n}$ and $\boldsymbol{t}$ are, respectively, a unit normal and a unit tangent vector to the surface. Equation (15) implies that there is no frictional force acting at the contact surface, and the boundary condition (16) ensures that there is no interpenetration of the target material into the penetrator and vice-versa. A partial justification for boundary condition (15) is that a thin layer of material at the interface either melts or is severely degraded by adiabatic shear. At points far away from the penetrator, we impose

$$|\boldsymbol{v} + \boldsymbol{e}| \to 0, \quad \text{as} \quad (r^2 + z^2)^{1/2} \to \infty, \quad z > -\infty, \tag{17}$$

$$|\boldsymbol{\sigma n}| \to 0, \quad \text{as} \quad z \to -\infty, \quad r \geqq 1, \tag{18}$$

where $\boldsymbol{e}$ is a unit vector in the positive z-direction. The boundary condition (17) embodies the assumption that target particles far from the penetrator and not on the bounding back surface appear to be moving at a uniform velocity with respect to it. Equation (18) implies that when a target particle has moved far to the rear of the penetrator, the surface tractions on it vanish.

The problem formulation outlined above differs from that studied earlier by Batra and co-workers [25]–[30] because of the consideration of elastic deformations here. In earlier work substitution for $\boldsymbol{s}$ in Eq. (12) resulted in non-linear field equations for $\boldsymbol{v}$. Here, Eq. (13) can not be solved easily for $\boldsymbol{s}$; accordingly we solve Eqs. (11)–(13) for p, $\boldsymbol{v}$ and $\boldsymbol{s}$. This necessitates that the boundary conditions for stress components be prescribed at the entrance region. Shimazaki and Thompson [31] have studied a simple problem whose governing equations are similar to Eqs. (11)–(13), and have justified prescribing p and $\boldsymbol{s}$ at the entrance region.

3 Finite element formulation of the problem

Unless we use special infinite elements, a numerical solution of the problem requires that we consider a finite region. Accordingly, we study deformations of the region R shown in Fig. 1, and replace boundary conditions (17) and (18) at the far surfaces by the following conditions (19) and (21) on the boundary surfaces of the finite region being analyzed:

$$v_r = 0, \quad v_z = -1.0 \quad \text{on the bounding surface } EFA, \tag{19}$$

$$\sigma_{rz} = 0, \quad v_r = 0 \quad \text{on the axis of symmetry } DE, \tag{20}$$

$$\sigma_{zz} = 0, \quad v_r = 0 \quad \text{on the surface } AB. \tag{21}$$

Conditions (20) follow from the assumed axisymmetric nature of deformations. The validity of replacing (17) by (19), (18) by (21), and the accuracy of the computed results depend upon the size of the region R. Since Eq. (13) can not be solved explicitly for $\boldsymbol{s}$, but is to be solved simultaneously with Eqs. (11) and (12), we need to specify the state of stress of the material entering the control volume (e.g. see Shimazaki and Thompson [31]). Accordingly we set

$$p = 0, \quad s_{rr} = 0, \quad s_{\theta\theta} = 0, \quad s_{zz} = 0 \quad \text{and } s_{rz} = 0 \quad \text{on the boundary surface } EFA. \tag{22}$$

The first step in analyzing the problem numerically is to obtain a weak formulation of the problem. Let $\boldsymbol{\phi}$ and $\boldsymbol{\psi}$ be smooth and bounded vector and tensor-valued functions defined on the region R that vanish on the surface EFA, and $\phi_r = 0$ on AB and DE, $\boldsymbol{\phi} \cdot \boldsymbol{n} = 0$ on the target/penetrator interface BCD. Also, let η be a bounded, scalar valued function defined on R. Taking the inner product of both sides of Eqs. (11), (12), and (13) with η, $\boldsymbol{\phi}$ and $\boldsymbol{\psi}$, integrating the

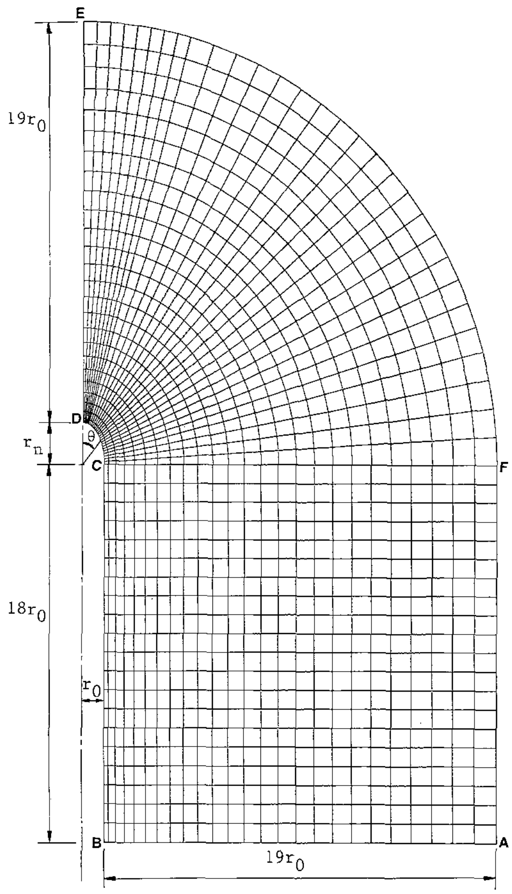

Fig. 1. The finite region studied and its discretization

resulting equations over R, using the divergence theorem, the traction boundary conditions (15), (19) and (20), and the aforestated boundary conditions on ϕ and ψ, we arrive at the following equations:

$$\int \eta(\operatorname{div} \boldsymbol{v})\, dV = 0, \tag{23}$$

$$\int p(\operatorname{div} \boldsymbol{\phi})\, dV - \int \boldsymbol{s} : \left(\operatorname{grad} \boldsymbol{\phi} + (\operatorname{grad} \boldsymbol{\phi})^T\right) dV = \alpha \int [(\boldsymbol{v} \cdot \operatorname{grad})\, \boldsymbol{v}] \cdot \boldsymbol{\phi}\, dV, \tag{24}$$

$$\int \boldsymbol{\psi} : \bar{\boldsymbol{s}}\, dV = \frac{1}{2} \int \beta(I)\, \boldsymbol{\psi} \colon [\operatorname{grad} \boldsymbol{v} + (\operatorname{grad} \boldsymbol{v})^T]\, dV, \tag{25}$$

$$\bar{\boldsymbol{s}} = \boldsymbol{s} + \beta\gamma\big((\boldsymbol{v} \cdot \operatorname{grad})\, \boldsymbol{s} + \boldsymbol{sW} - \boldsymbol{Ws}\big). \tag{26}$$

Here and below the integrations are over the region R. The boundary value problem defined by Eqs. (11)–(13), (15), (16), and (19)–(22) is equivalent to the statement that $\boldsymbol{v}$ and $\boldsymbol{s}$ satisfy the prescribed essential boundary conditions and Eqs. (23)–(25) hold for every $\boldsymbol{\phi}$, $\boldsymbol{\psi}$ and η such that grad $\boldsymbol{\phi}$, grad $\boldsymbol{\psi}$, and η are square integrable over R, and $\boldsymbol{\phi}$ and $\boldsymbol{\psi}$ satisfy the stated homogeneous essential boundary conditions.

An approximate solution of Eqs. (23)–(25) has been obtained by using the finite element method (e.g. see Hughes [32]). In order to preclude spurious oscillations in the stress deviator $\boldsymbol{s}$ and also to improve upon the rate of convergence, we employed the Petrov-Galerkin approximation of Eq. (25) but Galerkin approximation of Eqs. (23) and (24) (see Hughes [32]). The region R is divided into quadrilateral subregions, called finite elements, over each of which

$\boldsymbol{v}$ and $\boldsymbol{s}$ are approximated by simple polynomials defined in terms of their values at the four corner nodes. The pressure p is assumed to be uniform over each element; this value is assigned to the centroid of the element. The basis functions used in the Petrov-Galerkin approximation are those given by Brooks and Hughes [33]. The boundary condition (16) on target/penetrator interface BCD is enforced by using the method of Lagrange multipliers.

We note that Eqs. (23)–(25) are coupled and are nonlinear in $\boldsymbol{v}$. The following iterative technique was used to linearize them:

$$\int \eta(\operatorname{div} \boldsymbol{v}^m)\, dV = 0, \tag{27}$$

$$\int p^m(\operatorname{div} \boldsymbol{\phi})\, dV - \int \boldsymbol{s}(\boldsymbol{v}^{m-1}) : \left(\operatorname{grad} \boldsymbol{\phi} + (\operatorname{grad} \boldsymbol{\phi})^T\right) dV = \alpha \int \left((\boldsymbol{v}^{m-1} \cdot \operatorname{grad})\, \boldsymbol{v}^m\right) \cdot \boldsymbol{\phi}\, dV, \tag{28}$$

$$\int \boldsymbol{\psi} : \boldsymbol{s}\, dV + \int \boldsymbol{\psi} : \bar{\boldsymbol{s}}(\boldsymbol{v}^{m-1})\, dV = \int \beta(I^{m-1})\, \boldsymbol{\psi} : [\operatorname{grad} \boldsymbol{v}^{m-1} + (\operatorname{grad} \boldsymbol{v}^{m-1})^T]\, dV, \tag{29}$$

where m is the iteration number. The iterative process was stopped when

$$\left(\sum \|\boldsymbol{v}^m - \boldsymbol{v}^{m-1}\|^2\right)^{1/2} \leqq 0.01\left(\sum \|\boldsymbol{v}^{m-1}\|^2\right)^{1/2}, \tag{30.1}$$

$$\left(\sum |p^m - p^{m-1}|^2\right)^{1/2} \leqq 0.01\left(\sum |p^{m-1}|^2\right)^{1/2}, \tag{30.2}$$

$$\left(\sum \|\boldsymbol{s}^m - \boldsymbol{s}^{m-1}\|^2\right)^{1/2} \leqq 0.01\left(\sum \|\boldsymbol{s}^{m-1}\|^2\right)^{1/2}, \tag{30.3}$$

where $\|\boldsymbol{v}\|^2 = v_r^2 + v_z^2$, and $\|\boldsymbol{s}\|^2 = \operatorname{tr}(\boldsymbol{s}\boldsymbol{s}^T)$. The summation sign refers to the sum of the indicated quantity evaluated at all nodes in the finite element mesh. This convergence criterion is weaker than the local norm used by Batra and his co-workers [25]–[30].

Having determined pressure $\bar{p}$ at the centroids of elements, the pressure at node points is computed from

$$\sum_{j=1}^{M} \left(\int N_i N_j\, dV\right) p_j\, dV = \int N_i \bar{p}\, dV, \qquad i = 1, 2, \ldots, M \tag{31}$$

where M is the number of nodes, and $N_1, N_2, \ldots$ are the piecewise bilinear finite element basis functions. We note that Eq. (31) also serves to smooth out the pressure field.

4 Computation and discussion of results

A computer code based on Eqs. (27)–(29) and employing 4-noded quadrilateral elements has been developed. The two components (v_r, v_z) of the velocity and four components (s_{rr}, $s_{\Theta\Theta}$, s_{rz}, and s_{zz}) of the deviatoric stress tensor are taken as unknowns at each node, and the hydrostatic pressure p is assumed to be constant within an element. The validity of the computer code was established by solving the radial flow problem discussed by Shimazaki and Thompson [31]. For the same finite element grid and numerical values of parameters as those used by Shimazaki and Thompson [31], the two sets of computed results plotted in Fig. 2 agree well with each other. Another test problem studied was a hypothetical one involving the flow of a Navier-Stokes fluid in a circular pipe and achieving a favorable comparison between the computed and analytical results; this problem is discussed in the Appendix.

In the results presented below, the target material was assumed to be an aluminium-alloy for which we took $\sigma_0 = 340$ MPa, $G = 27$ GPa, and $\varrho = 2\,890$ kg/m^3. However, the results are presented below in terms of non-dimensional numbers and are therefore valid for other

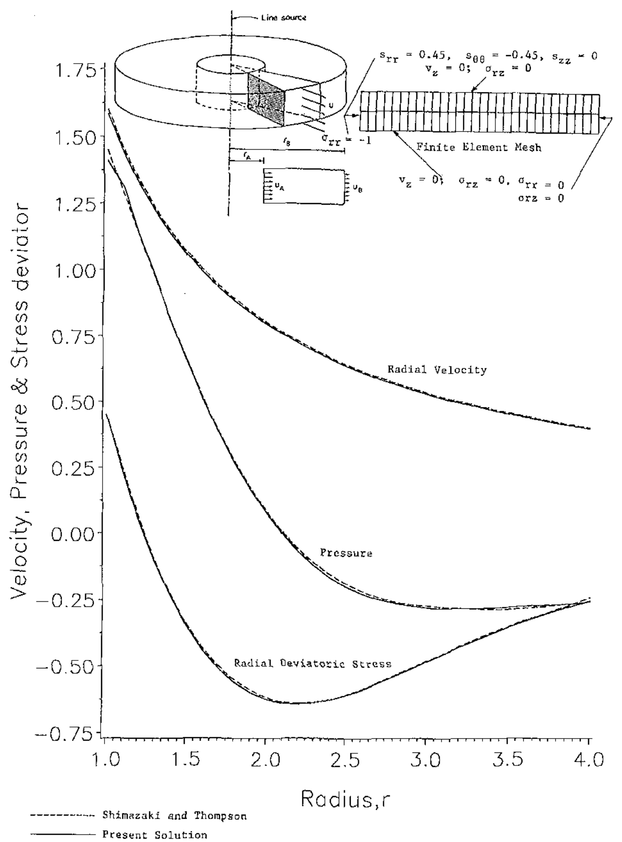

Fig. 2. Comparison of the presently computed solution with that of Shimazaki and Thompson for the radial flow problem

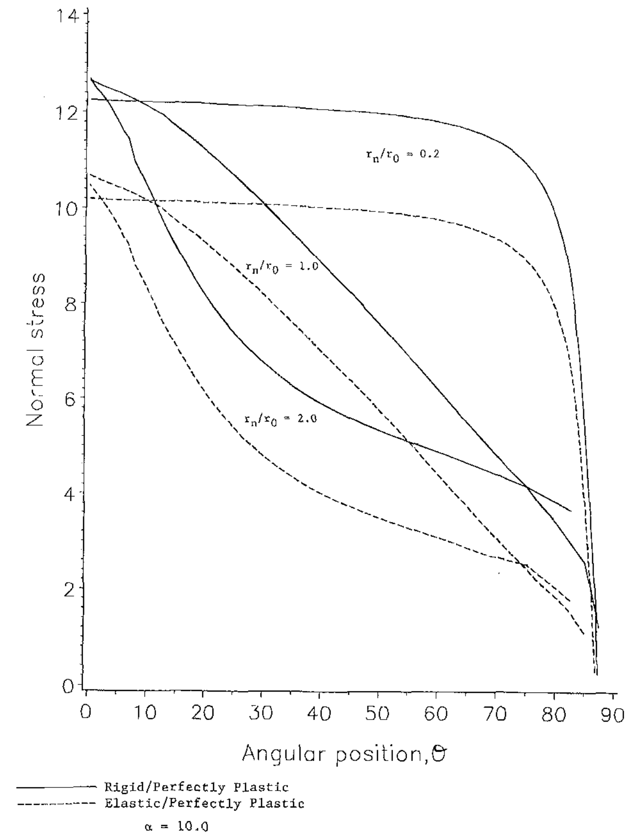

Fig. 3. Distribution of the compressive normal stress on the penetrator nose surface for three different nose shapes and when the target material is modeled as elastic perfectly plastic and as rigid perfectly plastic. $\alpha = 10$

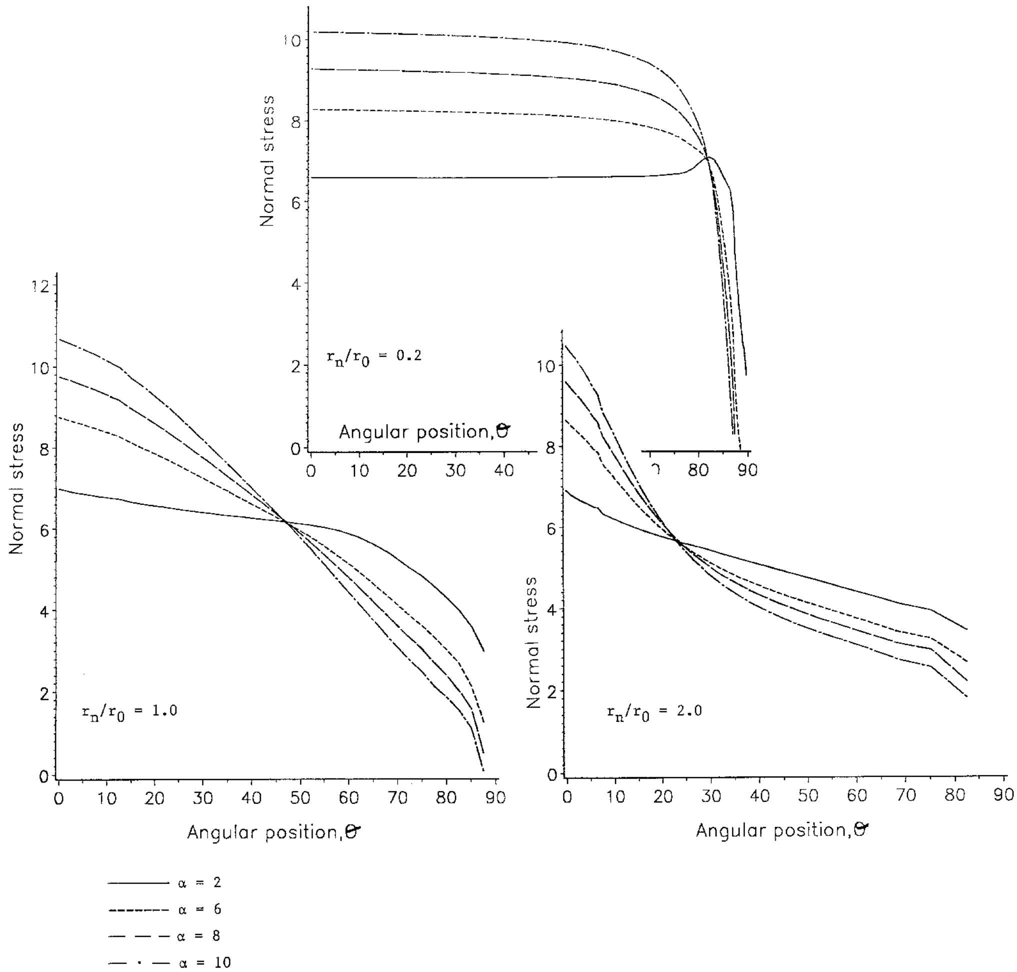

Fig. 4. Distribution of the compressive normal stress on the penetrator nose surface for the three different nose shapes and for $\alpha = 2$, 6, 8, and 10 when the target material is modeled as elastic perfectly plastic

combinations of target material and penetration speed. The finite element subdivision of the target region when the penetrator has an ellipsoidal nose with $r_n/r_0 = 2.0$ is shown in Fig. 1. The components of the deviatoric stress tensor and the hydrostatic pressure were assigned to be zero at the entrance region EFA.

Figure 3 depicts the effect of material elasticity ($\gamma = 1.26 \times 10^{-2}$) on the pressure distribution at the nose surface for three different nose shapes with $r_n/r_0 = 0.2$, 1.0, and 2.0, and when α was set equal to 10.0. For each nose shape the normal pressure on the nose surface was lower when material elasticity was accounted for than that for the rigid perfectly plastic case ($\gamma = 0$). However, the general shapes of the curves are unaffected by the consideration of elastic effects. The normal stress at the stagnation point is nearly the same for the three nose shapes, but the shape of the normal stress versus angular position θ curve depends strongly upon the nose shape. As expected, for the blunt nose, the normal stress stays constant over most of the nose surface, and drops off rapidly to zero near the nose periphery. For the hemispherical nosed penetrator, the normal stress drops off nearly evenly as one moves away from the center to the

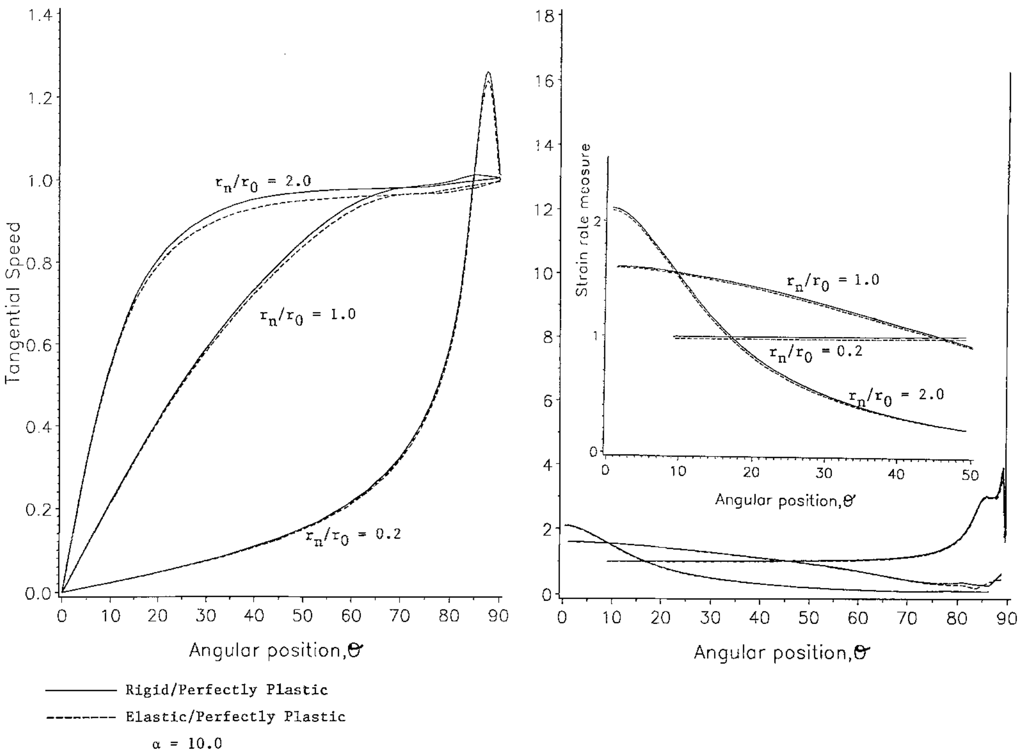

Fig. 5. Distribution of the tangential speed and the strain-rate measure I upon the penetrator nose surface for three different nose shapes; $\alpha = 10$

nose periphery. For the ellipsoidal nosed penetrator the normal stress drops off quite rapidly for $0° \leqq \theta \leqq 30°$, and rather slowly for $\theta > 30°$. The curvature of the curve for $r_n/r_0 = 2.0$ is opposite to that of the curve for $r_n/r_0 = 1.0$ or 0.2.

The distribution of the compressive normal stress on the nose surface for $\alpha = 2$, 6, 8, and 10 and when the target material is modeled as elastic perfectly plastic is plotted in Fig. 4. For each of the three nose shapes considered the normal stress at points on the nose surface for which $0 \leqq \theta \leqq \theta_c$ increases with α, that at points with $\theta > \theta_c$ decreases with α. The value of θ_c equals approximately 22°, 45°, and 82°, for the long tapered ellipsoidal nosed, hemispherical nosed and the blunt nosed penetrators, respectively. The normal stress at points near the nose periphery was found to be positive for $\alpha > 15$ implying thereby that the target particles tended to separate away from the penetrator. However, for the blunt nosed penetrator this tendency of the target particles to separate away from the penetrator adjacent to the nose periphery was also observed at lower values of α.

The distribution of the tangential speed on the penetrator nose surface and the strain-rate measure I at the centroids of elements abutting the penetrator nose surface for the three different nose shapes and $\alpha = 10.0$ is shown in Fig. 5. It is apparent that the material elasticity has negligible effect on the tangential speed and the strain-rate measure I. For the long tapered nosed penetrator, the tangential speed increases very rapidly for $0 \leq \theta \leq 20°$, attains the value of 1.0 at $\theta \approx 30°$, and then stays close to 1.0 for $30° \leq \theta \leq 90°$. For the hemispherical nosed penetrator the tangential speed increases gradually from 0 at $\theta = 0°$ to 1.0 at $\theta \approx 60°$ and does not vary much for $60° < \theta \leqq 90°$. The trend is quite different for the blunt nosed penetrator. In this case the

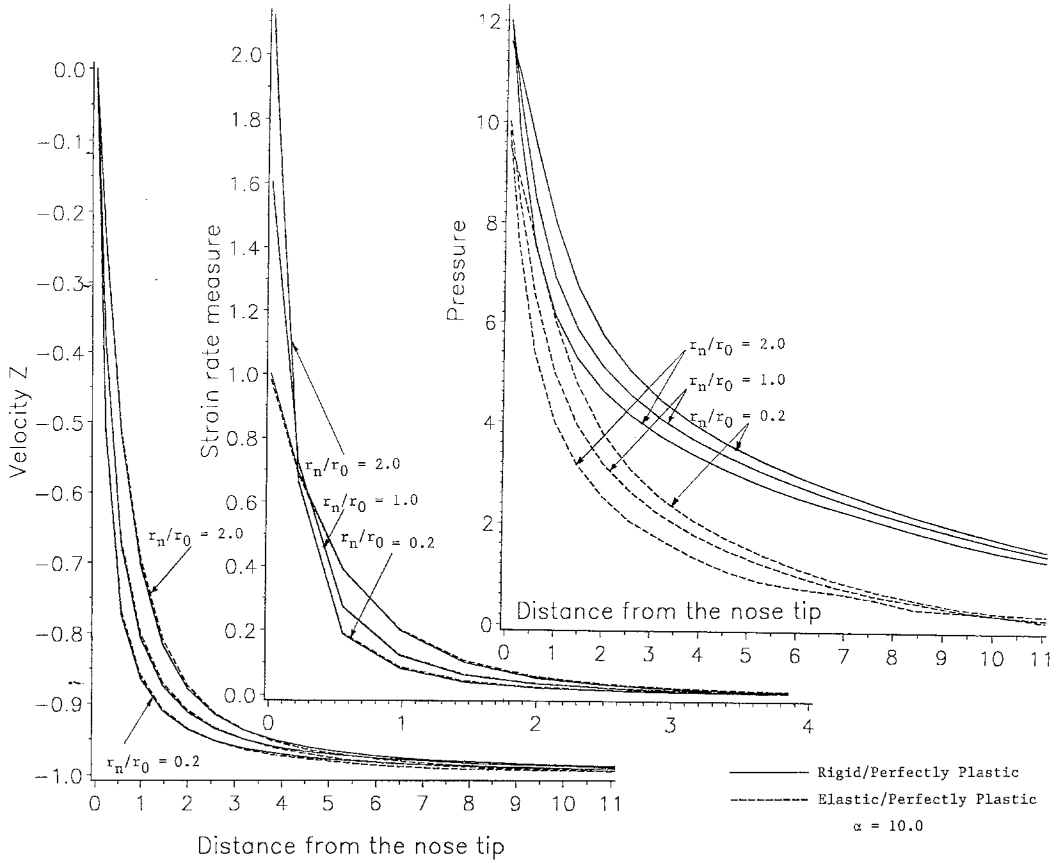

Fig. 6. Variation of the pressure, strain-rate measure I and the z-velocity on the axial line with the distance from the penetrator nose tip

tangential speed increases slowly for $\theta \leqq 50°$, and then very rapidly. The maximum value of the tangential speed computed for the blunt nosed penetrator is more than that for the other two nose shapes. For the blunt nosed penetrator the peak values of the strain-rate measure I are an order of magnitude higher than that for the long tapered nosed penetrator. Whereas $I_{\max}$ occurs near the nose periphery for the blunt nosed penetrator, peak values of I for the other two nose shapes are realized at the stagnation point. Both for the hemispherical and the elliptical nosed penetrator, I decreases slowly from its maximum value at the nose center to nearly zero at the nose periphery.

We have plotted the variation of the hydrostatic pressure, strain-rate measure I and the axial velocity along the axis of symmetry in Fig. 6. The consideration of material elasticity has very little effect on the distribution of I and the axial velocity but reduces noticeably the value of the hydrostatic pressure. The value of I at the stagnation point is maximum for the ellipsoidal nosed penetrator and least for the blunt nosed penetrator; the former equals nearly twice the latter. It is clear that severe deformations of the target occur at points situated at most $3r_0$ from the penetrator nose surface. Thus the target region studied is adequate. The pressure drops off more slowly when the target material is modeled as rigid perfectly plastic as compared to the case when it is modeled as elastic perfectly plastic. The general shapes of the curves I, v_z or p versus the distance from the nose tip are unaffected by the penetrator nose shape and by the consideration of material elasticity.

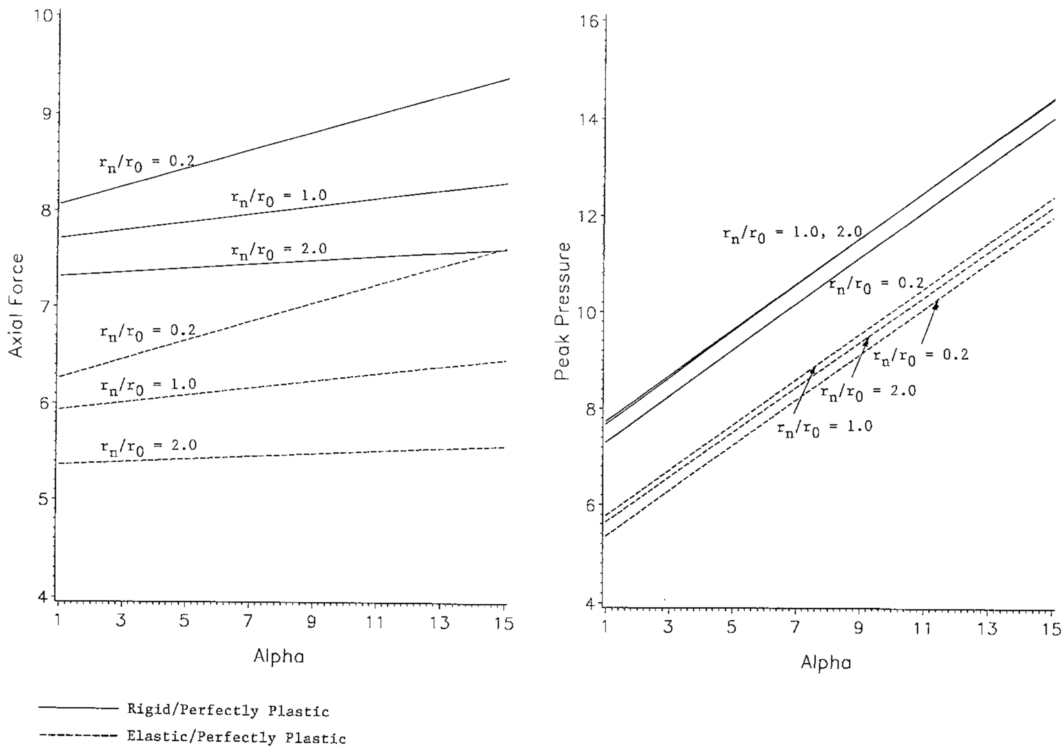

Fig. 7. Dependence of the peak pressure at the stagnation point and the axial resisting force experienced by the penetrator upon α

The dependence of the peak pressure that occurs at the stagnation point, and of the axial resisting force F experienced by the penetrator upon α is depicted in Fig. 7. The axial resisting force F is given by

$$F = 2 \int_0^{\pi/2} (\boldsymbol{n} \cdot \boldsymbol{\sigma n}) \frac{\cos\phi \ \sin\theta \ [\sin^2\theta + (1/r_n)^4 \ \cos^2\theta]^{1/2}}{[\sin^2\theta + (1/r_n)^2 \ \cos^2\theta]^2} \, d\theta, \tag{32.1}$$

$$\cos\phi = \frac{z/r_n{}^2}{[r^2 + (z/r_n{}^2)^2]^{1/2}}, \tag{32.2}$$

where the angle θ is defined in Fig. 1 and (r, z) are the coordinates of a point on the penetrator/target interface. The corresponding axial force in physical units is given by $(\pi r_0{}^2 \sigma_0) F$. For each nose shape, the relationships between $p_{\max}$ and α, and F and α are nearly affine, and the consideration of elastic effects lowers the value of $p_{\max}$ by about 2, and of F by 1.8. The least squares fit to the computed data gives

$$p_{\max} = 6.82 + 0.48\alpha, \quad F = 7.97 + 0.094\alpha, \quad r_n/r_0 = 0.2, \tag{33.1}$$

$$p_{\max} = 7.20 + 0.48\alpha, \quad F = 7.67 + 0.042\alpha, \quad r_n/r_0 = 1.0, \tag{33.2}$$

$$p_{\max} = 7.26 + 0.48\alpha, \quad F = 7.29 + 0.021\alpha, \quad r_n/r_0 = 2.0, \tag{33.3}$$

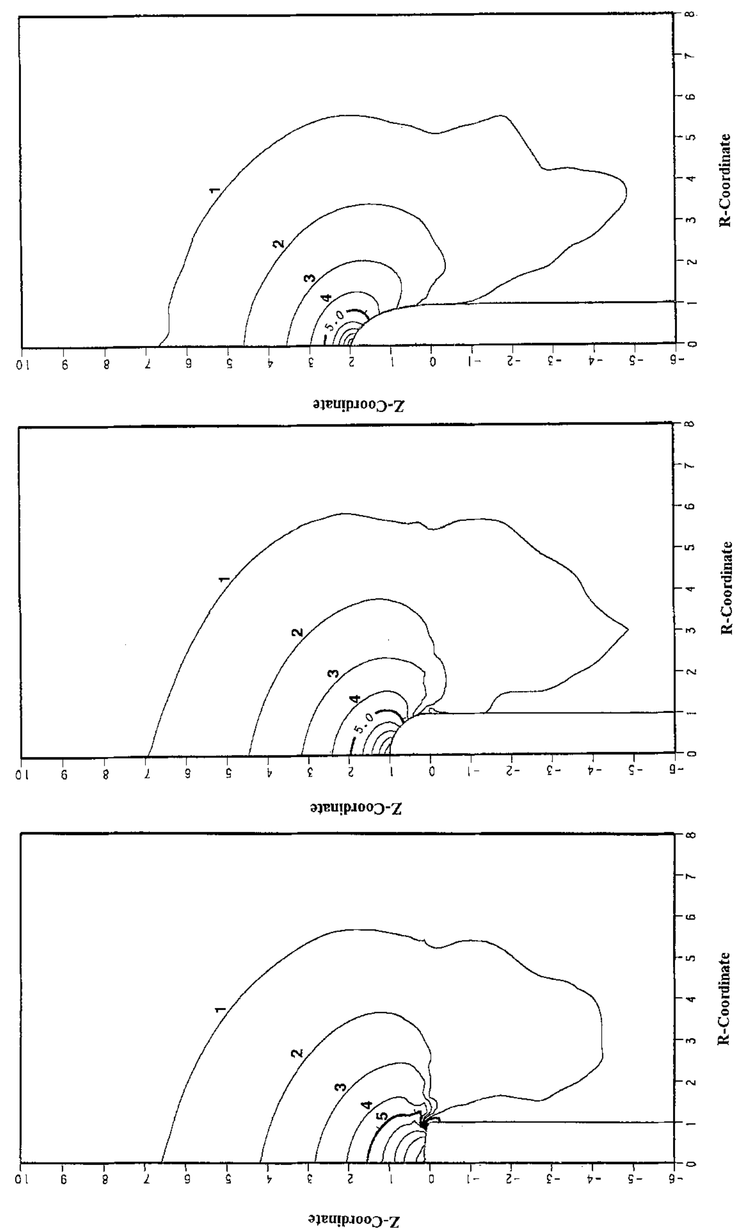

Fig. 8. Contours of the hydrostatic pressure in the deforming target region for three different nose shapes, $\alpha = 10$

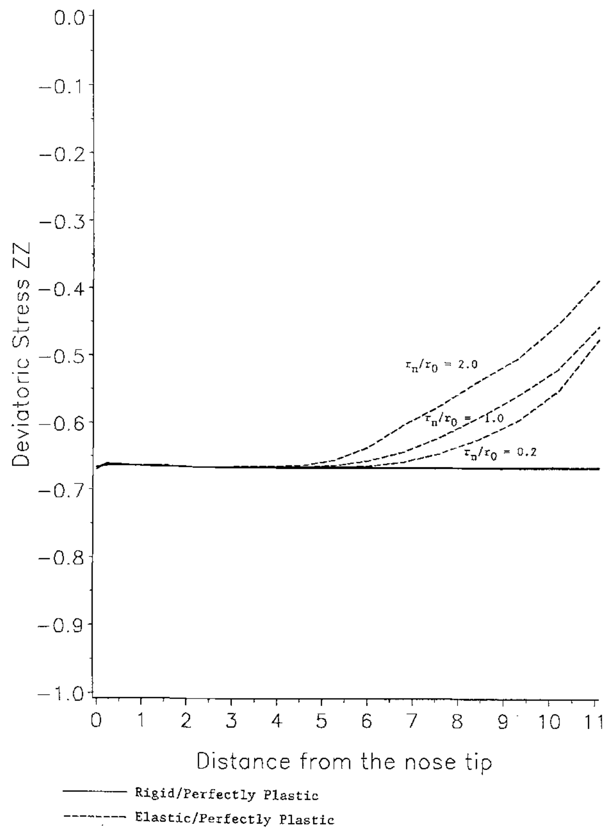

Fig. 9. Variation of the deviatoric stress s_{zz} on the axial line

when the target material is modeled as rigid perfectly plastic, and

$$p_{\max} = 4.87 + 0.47\alpha, \quad F = 6.17 + 0.096\alpha, \quad r_n/r_0 = 0.2, \tag{34.1}$$

$$p_{\max} = 5.29 + 0.47\alpha, \quad F = 5.90 + 0.038\alpha, \quad r_n/r_0 = 1.0, \tag{34.2}$$

$$p_{\max} = 5.16 + 0.47\alpha, \quad F = 5.32 + 0.019\alpha, \quad r_n/r_0 = 2.0, \tag{34.3}$$

when it is taken to be elastic perfectly plastic. We note that the dependence of F upon α is quite weak.

The contours of the hydrostatic pressure in the deforming target region for the three different nose shapes and $\alpha = 10$ are depicted in Fig. 8. These show that the pressure falls off to zero, not only on the axial line, but also along other radial lines as one moves away from the penetrator nose surface. The contour of the zero hydrostatic pressure near the bounding surface is not plotted in order to focus on the narrow region surrounding the penetrator/target interface. For each one of the three nose shapes examined, the pressure near the nose periphery drops off to a very small value. The pressure gradient at points near the nose tip is steepest for the ellipsoidal nosed penetrator.

On the axial line uniaxial strain conditions prevail approximately. Thus the magnitude of the deviatoric stress s_{zz} at a point on the axial line should equal $(2/3\sigma_0)$ whenever the material point is deforming plastically. For a rigid perfectly plastic target material and for each nose shape considered, the computed value of $|s_{zz}|$ came out to be $2/3\sigma_0$ as shown in Fig. 9. Near the boundary point F of the target region studied, $|s_{zz}|$ rapidly dropped to the prescribed zero value. This rapid drop is not shown in the figure. However, when the target material is modeled as elastic perfectly plastic, $|s_{zz}|$ equals $(2/3\sigma_0)$ for a distance of $3r_0$ to $4r_0$ from the nose tip and then gradually decreases to the assigned value of zero at the outer boundary. The penetrator nose shape influences the rate of decay of $|s_{zz}|$; the plastic deformation progresses farther for the blunt nosed penetrator and $|s_{zz}|$ decays slowly for it as compared to the ellipsoidal nosed penetrator. On the axial line, the Bernoulli equation in terms of non-dimensional variables and as modified by Tate [17], [18] is

$$\frac{1}{2}\alpha + R_t = -\sigma_{zz}^s = p^s + \frac{2}{3} \tag{35}$$

where R_t accounts for the strength of the target material, and σ_{zz}^s and p^s are the values of σ_{zz} and p at the stagnation point. Having computed σ_{zz} and knowing α, we can find R_t. For the three nose shapes considered, the least squares fit to the computed values of R_t for different values of α gives the following:

$$R_t = 7.48 - 0.020\alpha, \quad (r_n/r_0) = 0.2, \tag{36.1}$$

$$R_t = 7.86 - 0.018\alpha, \quad (r_n/r_0) = 1.0, \tag{36.2}$$

$$R_t = 7.92 - 0.024\alpha, \quad (r_n/r_0) = 2.0, \tag{36.3}$$

for a rigid perfectly plastic target, and

$$R_t = 5.53 - 0.027\alpha, \quad (r_n/r_0) = 0.2, \tag{37.1}$$

$$R_t = 5.96 - 0.027\alpha, \quad (r_n/r_0) = 1.0, \tag{37.2}$$

$$R_t = 5.83 - 0.032\alpha, \quad (r_n/r_0) = 2.0, \tag{37.3}$$

for an elastic perfectly plastic target. In either case the dependence of R_t upon α is very weak and this explains why the assumption of constant R_t in simpler theories of penetration gives good results. Tate [19] has proposed that

$$R_t = \frac{2}{3} + \ln\left(\frac{2E_t}{3\sigma_0}\right), \tag{38}$$

where E_t is Young's modulus of the target material. Thus for values of G and σ_0 taken herein,

$$R_t = \frac{2}{3} + \ln\left(\frac{2}{3}\left(\frac{3 \times 27 \times 10^9}{0.34 \times 10^9}\right)\right) = 5.734 \tag{39}$$

which is close to the values computed for the elastic perfectly plastic target. Recalling that $p^s = p_{\max}$, it is interesting to note that the slope of the least squares fit to the $p_{\max}$ vs. α data is close to 0.5 as it should be if Eq. (35) were to hold.

As is transparent from Fig. 9 the stress state at target particles far away from the target/penetrator interface lies inside the surface defined by

$$\operatorname{tr}(s^2) = \frac{2}{3}. \tag{40}$$

This is certainly true of points on the boundary surface EFA where $\boldsymbol{s} = \boldsymbol{0}$ is prescribed. The constitutive assumptions (4)–(6) tacitly assume that each target particle is deforming elastically and plastically. However, points where $\|\boldsymbol{s}\|$ is small are undergoing negligible plastic deforma-

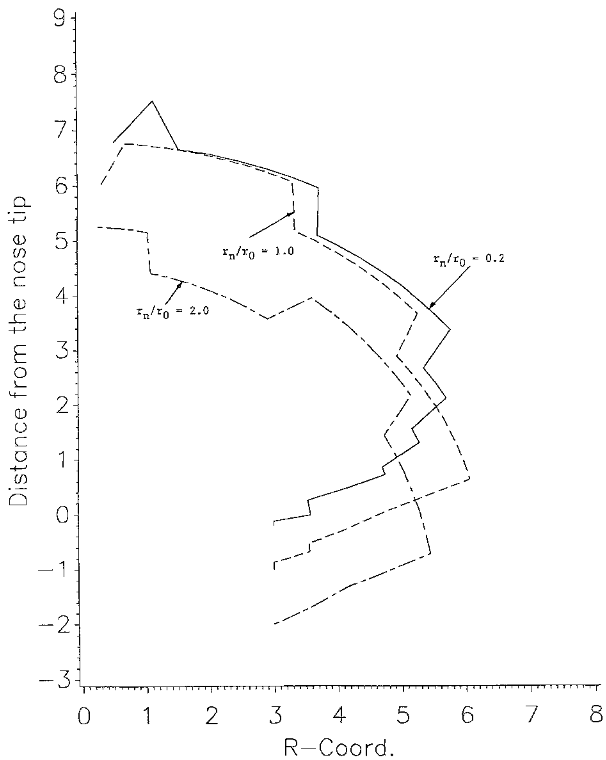

Fig. 10. Elastic-plastic boundary for three different nose shapes, and $\alpha = 10$

tions. Here we classify points for which the stress state satisfies the condition (40) as deforming plastically and those for which the stress state lies inside the surface (40) as deforming elastically. The elastic plastic boundary computed by using this criterion and obtained by joining points that are deforming plastically by straight line segments is depicted in Fig. 10.These curves suggest that less of the material ahead of the penetrator nose tip and to the sides of the rigid rod is deformed plastically for the ellipsoidal nosed penetrator as compared to the other two nose shapes considered. The distance of the elastic-plastic boundary from the penetrator nose tip is found to be 5.4, 6.8, and 7.7, respectively, according as the penetrator nose shape is ellipsoidal, hemispherical or blunt. Tate [19] presumed that a material particle was deforming either elastically or plastically and based on his solenoid flow model he found the axial distance of the elastic-plastic boundary from the stagnation point to be 6.71, which compares well with our computed values. The computed results, not plotted herein, show that ahead of the penetrator the elastic-plastic boundary does not advance much when α is increased from 6 to 10 for the hemispherical and blunt nosed penetrator but does move appreciably for the ellipsoidal nosed penetrator. As soon as a material particle goes past the nose periphery, stresses on it are relieved and the stress state for it lies inside the surface defined by (40).

A measure of the deformation of a material particle is the value of the effective strain ε, defined as

$$\dot{\varepsilon} = \left(\frac{1}{2}\,\mathrm{tr}\,\boldsymbol{D}^2\right)^{1/2} = I \tag{41}$$

at that point. For a steady state penetration problem Tate [20] has described a method to compute different components of the finite strain tensor from a knowledge of the velocity field. He showed that contours of the circumferential strain are approximately parallel to the crater

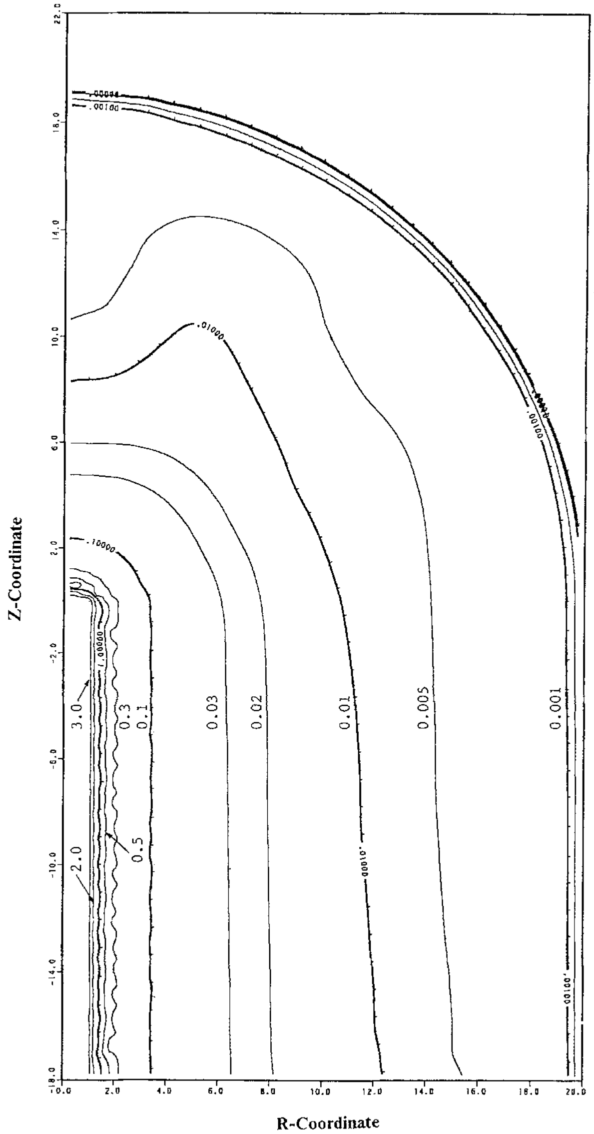

Fig. 11. Contours of the effective strain in the deforming target region for a blunt nosed penetrator, and $\alpha = 10$

surface and that the circumferential strain at a point distance a little more than one radius from the crater tip equals 5%. Because of the steady state deformations, we write Eq. (41) as

$$(\boldsymbol{v} \cdot \mathrm{grad})\, \varepsilon = I \tag{42}$$

and first compute I from the velocity field, and then find ε as a solution of Eq. (42) with the boundary condition $\varepsilon = 0$ on EFA. These contours basically look alike for the three nose shapes, and are shown in Fig. 11 only for the blunt nosed penetrator. The contours of ε suggest that severe deformations propagate farther to the side than ahead of the penetrator nose. The peak values of ε occur at target particles near the target/penetrator interface and equal 100%. We recall that no failure or fracture criterion is included in our work. Thus a material point can undergo an unlimited amount of deformation. As expected, the strain gradients are high at points near the target/penetrator interface and rapidly decay as one moves away from this interface.

5 Conclusions

We have analyzed the steady state axisymmetric deformations of an elastic perfectly plastic target being penetrated by a fast moving rigid cylindrical rod. Three different nose shapes, i.e., ellipsoidal, hemispherical, and blunt are considered. For each nose shape the effect of the penetration speed upon the deformations of the target is investigated. The consideration of elastic effects necessitates that the problem be analyzed by using a mixed formulation in which both velocities and stresses at a node point are taken as unknowns.

The peak hydrostatic pressure at the stagnation point is lower when elastic effects are included than when they are not. Also, the axial resisting force experienced by the penetrator is found to be lower when the target material is modeled as elastic perfectly plastic than when it is modeled as rigid perfectly plastic. In either case, the axial force depends upon the non-dimensional parameter α very weakly. Similarly the strength parameter appearing in the modified Bernoulli equation is found to be essentially independent of α, and the computed value is close to that given by Tate. For the blunt nosed penetrator, plastic deformations spread farther ahead of the penetrator nose as well as to its sides as compared to those when the penetrator nose is ellipsoidal or hemispherical. The distance of the elastic-plastic boundary from the penetrator nose tip along the axis of symmetry is found to compare well with that estimated by Tate.

Appendix

One of the problems analyzed in order to establish the validity of the finite element code developed is the following hypothetical problem. Consider the flow of a homogeneous and incompressible Navier-Stokes fluid of unit mass density and unit viscosity. The flow is governed by equations obtained from Eqs. (1) through (8) when $\varrho = 1$, $\sigma_0/\sqrt{3}\, I = 2$, omitting Eq. (4) and adding the body force vector to the left-hand side of Eq. (2). These equations have the solution

$$v_r = r(1-r), \qquad v_z = -z(2-3r), \qquad p = z, \tag{A1}$$

$$g_r = 3 + r(1-r)(1-2r), \qquad g_z = 1 - 3z/r + 3zr(1-r) + z(2-3r)^2, \tag{A2}$$

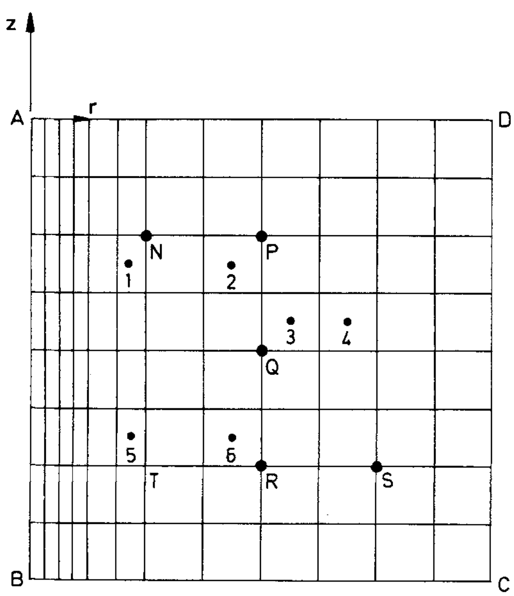

Fig. A 1. The finite element mesh used for the test problem

Table A 1. Comparison of analytical and numerical solution. The good agreement between the computed and analytical values of v_r, v_z, and p establishes the validity of the code

Point	Analytical values		Computed values		Point	Analytical value	Computed value
	v_r	v_z	v_r	v_z		$-p$	$-p$
N	0.1875	0.3125	0.1890	0.3116	1	0.3125	0.3311
P	0.2500	0.1250	0.2504	0.1250	2	0.3125	0.3115
Q	0.2500	0.2500	0.2502	0.2500	3	0.4375	0.4329
R	0.2500	0.3750	0.2501	0.3750	4	0.4375	0.4318
S	0.1875	−0.1875	0.1875	−0.1875	5	0.6875	0.7032
T	0.1875	0.9375	0.1876	0.9374	6	0.6875	0.6819

where v_r and v_z are, respectively, the radial and axial components of the velocity, and g_r and g_z equal the radial and axial components of the body force per unit mass.

The finite element mesh used to compute the solution is shown in Fig. A 1. On surfaces AB, BC, and CD, both v_r and v_z as given by Eq. (A 1) were prescribed, on the surface AD, v_r and the normal traction, equal to σ_{zz}, were specified. In this case, the specification of the state of stress at the entrance region was not needed. In Table A 1, we have listed the converged computed results and the values from the analytical solution (A 1) at various points in the domain. Recall that the pressure field is assumed to be constant within an element; this value is assigned to the centroid of the element. The pressure field at other points is interpolated from its values at the centroids of the elements.

Acknowledgements

This work was supported by the U.S. Army Research Office Contract DAAL-89-K-0050 to the University of Missouri-Rolla. Some of the computations were performed on the NSF sponsored supercomputer center at the University of Illinois at Urbana-Champaign.

References

[1] Backman, M. E., Goldsmith, W.: The mechanics of penetration of projectiles into targets. Int. J. Engng. Sci. **16**, 1–99 (1978).
[2] Wright, T. W., Frank, K.: Approaches to penetration problems. SMIRT Symposium, No. 14, Impact. Lausanne, Switzerland 1987.
[3] Anderson, C. E., Bodner, S. R.: The status of ballistic impact modelling. Int. J. Impact Engng. 7, 9–35 (1985).
[4] Zukas, J. A. et al.: Impact dynamics. New York: Wiley-Interscience 1982.
[5] Blazynski, T. Z.. In: Materials at high strain rates (Blazynski, T. Z., ed.) London, New York: Elsevier 1987.
[6] MaCauley, M.: Introduction to impact engineering. London, New York: Chapman and Hall 1987.
[7] Awerbuch, J.: Technion-Israel Institute of Technology. MED Report No. 28 (1970).
[8] Awerbuch, J., Bodner, S. R.: Analysis of the mechanics of perforation of projectiles in metallic plates. Int. J. Solids Struct. **10**, 671–684 (1974).
[9] Ravid, M., Bodner, S. R.: Dynamic perforation of viscoplastic plates by rigid projectiles. Int. J. Engng. Sci. **21**, 577–591 (1983).
[10] Ravid, M., Bodner, S. R., Holcman, I.: Analysis of very high speed impact. Int. J. Engng. Sci. **25**, 473–482 (1987).
[11] Forrestal, M. J., Okajima, K., Luk, V. K.: Penetration of 6061-T651 Aluminum targets with rigid long rods. J. Appl. Mech. **55**, 755–760 (1988).

[12] Batra, R. C., Chen, X.: An approximate analysis of steady state axisymmetric deformations of viscoplastic targets. Int. J. Engng. Sci. **28**, 1347–1358 (1990).
[13] Birkhoff, G., MacDougall, D. P., Pugh, E. M., Taylor, G.: Explosives with lined cavities. J. Appl. Phys. **19**, 563–582 (1948).
[14] Pack, D. C., Evans, W. M.: Penetration by high-velocity jets. Proc. Phys. Soc. Lond. B **64**, 298–310 (1951).
[15] Allen, W. A., Rogers, J. W.: Penetration of a rod into a semi-infinite target. J. Franklin Inst. **272**, 275–284 (1961).
[16] Alekseevskii, V. P.: Penetration of a rod into a target at high velocity. Comb. Expl. and Shock Waves **2**, 63–66 (1966). (Translation from Russian, Faraday Press, New York)
[17] Tate, A.: A theory for the deceleration of long rods after impact. J. Mech. Phys. Solids **15**, 387–399 (1967).
[18] Tate, A.: Further results in the theory of long rod penetration. J. Mech. Phys. Solids **17**, 141–150 (1969).
[19a] Tate, A.: Long rod penetration models. Part I. A flow field model for high speed long rod penetration. Int. J. Mech. Sci. **28**, 535–548 (1986).
[19b] Tate, A.: Long rod penetration models. Part II. Extensions to the hydrodynamic theory of penetration. Int. J. Mech. Sci. **28**, 599–612 (1986).
[20] Tate, A.: A simple hydrodynamic model for the strain field in a target by the penetration of a high speed long rod projectile. Int. J. Engng. Sci. **16**, 845–858 (1978).
[21] Pidsley, P. H.: A numerical study of long rod impact onto a large target. J. Mech. Phys. Solids **32**, 315–333 (1984).
[22] Batra, R. C., Gobinath, T.: Steady state axisymmetric deformations of a thermoviscoplastic rod penetrating a thick thermoviscoplastic target. Int. J. Impact Engng. **11**, 1–31 (1991).
[23] Gobinath, T., Batra, R. C.: A steady state axisymmetric penetration problem for rigid perfectly plastic materials. Int. J. Engng. Sci. **29**, 1315–1331 (1991).
[24] Batra, R. C., Wright, T. W.: Steady state penetration of rigid perfectly plastic targets. Int. J. Engng. Sci. **24**, 41–54 (1986).
[25] Batra, R. C.: Steady state penetration of viscoplastic targets. Int. J. Engng. Sci. **25**, 1131–1411 (1987).
[26] Batra, R. C.: Steady state penetration of thermoviscoplastic targets. Comp. Mech. **3**, 1–12 (1988).
[27] Batra, R. C., Lin, P. R.: Steady state deformations of a rigid perfectly plastic rod striking a rigid cavity. Int. J. Engng. Sci. **26**, 183–192 (1988).
[28] Batra, R. C., Lin, P. R.: Steady state axisymmetric deformations of a thermoviscoplastic rod striking a hemispherical rigid cavity. Int. J. Impact Engng. **8**, 99–113 (1989).
[29] Batra, R. C., Lin, P. R.: Histories of stress, temperature and spin in steady state deformations of a thermoviscoplastic rod striking a hemispherical rigid cavity. Int. J. Engng. Sci. **28**, 93–98 (1990).
[30] Lin, P. R., Batra, R. C.: Histories of stress, strain-rate, temperature, and spin in steady state penetration problems. Int. J. Engng. Sci. **27**, 1155–1165 (1989).
[31] Shimazaki, Y., Thompson, E. G.: Elasto visco-plastic flow with special attention to boundary conditions. Int. J. Num. Meth. Engng. **17**, 97–112 (1981).
[32] Hughes, T. J. R.: The finite element method. Linear static and dynamic problems. Englewood Cliffs: Prentice-Hall 1987.

Authors' address: R. Jayachandran and R. C. Batra, Department of Mechanical and Aerospace Engineering and Engineering Mechanics, University of Missouri-Rolla, Rolla, MO 65401, U.S.A.